



Since January 2020 Elsevier has created a COVID-19 resource centre with free information in English and Mandarin on the novel coronavirus COVID-19. The COVID-19 resource centre is hosted on Elsevier Connect, the company's public news and information website.

Elsevier hereby grants permission to make all its COVID-19-related research that is available on the COVID-19 resource centre - including this research content - immediately available in PubMed Central and other publicly funded repositories, such as the WHO COVID database with rights for unrestricted research re-use and analyses in any form or by any means with acknowledgement of the original source. These permissions are granted for free by Elsevier for as long as the COVID-19 resource centre remains active.



# How do three-layer surgical masks prevent SARS-CoV-2 aerosol transmission?

Ziyi Han<sup>a</sup>, Lina Wang<sup>b</sup>, Yueyan Liu<sup>a</sup>, Tatleung Chan<sup>c</sup>, Zhandong Shi<sup>d</sup>, Mingzhou Yu<sup>a,\*</sup>

<sup>a</sup> Laboratory of Aerosol Science and Technology, China Jiliang University, Hangzhou, China

<sup>b</sup> Shanghai Key Laboratory of Atmospheric Particle Pollution and Prevention, Department of Environmental Science and Engineering, Fudan University, Shanghai 200433, China

<sup>c</sup> Department of Mechanical Engineering, The Hong Kong Polytechnic University, Kowloon, Hong Kong Special Administrative Region

<sup>d</sup> Zhengzhou Tobacco Research of CNTC, Zhengzhou 450001, China

## ARTICLE INFO

### Keywords:

COVID-19

Surgical mask

Transmission

Filtration efficiency

Respiratory resistance

## ABSTRACT

The three-layer surgical mask was recognized by the World Health Organization as an effective-protection tool for reducing SARS-CoV-2 transmission during the COVID-19 pandemic; however, the contribution of each layer of this mask to the particle size-dependent filtration performance resistance remains unclear. Here, both experimental work and numerical simulation were conducted to study the role of each mask layer in particle size-dependent filtration and respiratory resistance. By using scanning electron microscopy images of a commercial three-layer mask, composed of two spun-bond and one melt-blown nonwoven polypropylene fabric layers, four representative models were constructed, in which the computational fluid dynamics of multiphase flow were performed. The pressure drop of all models under different flow conditions was measured next. Numerical simulation was then verified by comparing the experimental results in the present study and other theoretical works. The filtration efficiency of the spun-bond polypropylene nonwoven fabric layer was much lower than that of the melt-blown nonwoven polypropylene fabric layer for the particle diameter in the range of 0.1–2.0  $\mu\text{m}$ . Both the spun-bond and melt-blown nonwoven polypropylene fabric layers demonstrated extremely low filtration efficiency for particles was  $<0.3 \mu\text{m}$  in diameter, with the maximum filtration efficiency being only 30%. The present results may facilitate rational design of mask products in terms of layer number and structural design.

## 1. Introduction

December 2019 marked the beginning of the COVID-19 pandemic. COVID-19 is caused by the novel coronavirus SARS-CoV-2. During the pandemic, the World Health Organization (WHO) confirmed that SARS-CoV-2 transmission occurs via three main routes: respiratory fluid droplets, direct contact, and aerosol [1,2]. The use of face masks or respirators has been demonstrated to prevent COVID-19 transmission via all aforementioned routes [3]. This has led to the production of commercial masks (including surgical masks, N95 masks, and face shields) and homemade cloth masks as well as their use for public and personal health control measures at the largest scale for the first time in human history. Surgical masks, also known as medical masks, are used by the general public worldwide, specifically in East Asian countries, such as China, Japan, South Korea, and Vietnam [4]. A Duke University

research team confirmed that surgical masks are the second most effective type of mask in protecting against SARS-CoV-2 infection, with N95 masks being the most effective [5]. In January 2022, the U.S. Centers for Disease Control and Prevention (CDC) conceded that the efficacy of surgical masks in preventing SARS-CoV-2 is much greater than that of cloth masks.

The WHO provided a complete description of the ideal surgical mask structure on January 5, 2022: it should be composed of three layers of synthetic nonwoven materials and configured to have the filtration layers sandwiched in the middle [6]. Depending on the thickness of their layers, surgical masks vary in levels of fluid resistance and filtration they provide. Currently, the most popular type of surgical masks on the market comprises three layers: two spun-bond polypropylene nonwoven fabric layers (on the inside and outside) and a melt-blown nonwoven polypropylene fabric filter layer (in the middle) [7]. The inner and outer

\* Corresponding author.

E-mail address: [mzyu@cjl.u.edu.cn](mailto:mzyu@cjl.u.edu.cn) (M. Yu).

<https://doi.org/10.1016/j.seppur.2023.123574>

Received 15 January 2023; Received in revised form 27 February 2023; Accepted 8 March 2023

Available online 12 March 2023

1383-5866/© 2023 The Authors. Published by Elsevier B.V. This is an open access article under the CC BY license (<http://creativecommons.org/licenses/by/4.0/>).

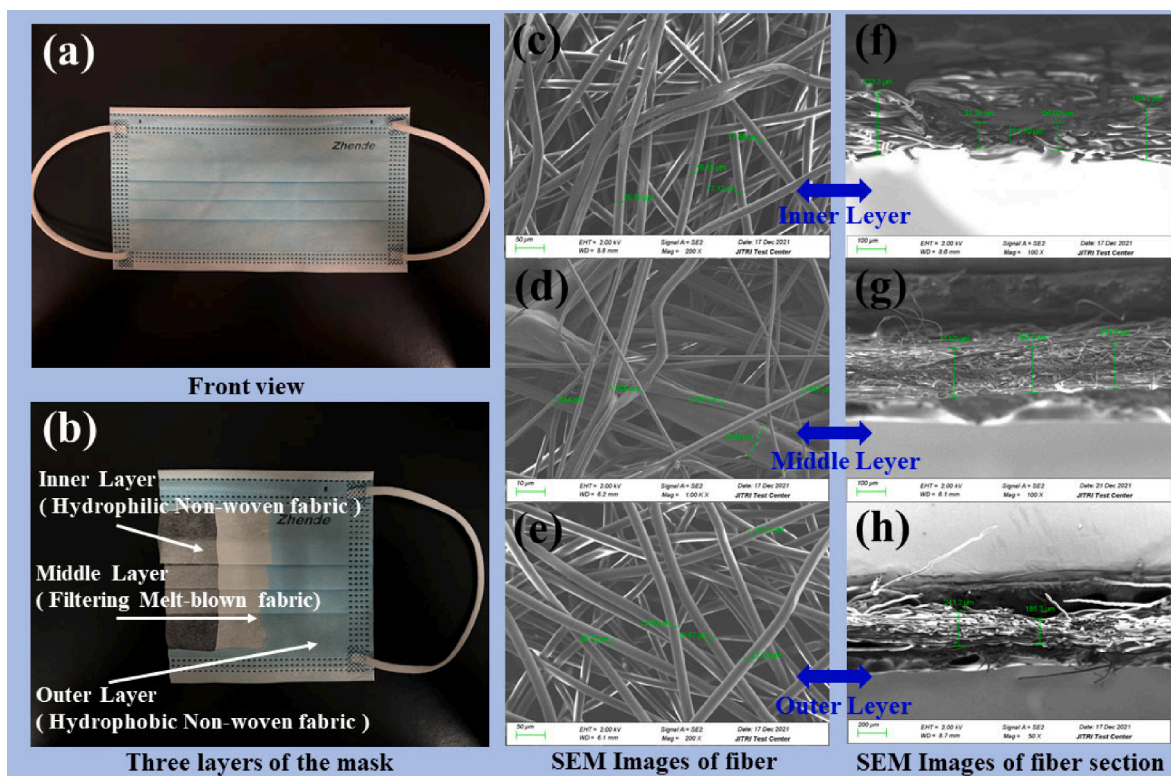


Fig. 1. Surgical mask, from Zhende Medical, used for modeling.

layers are designed to absorb and repulse the bodily fluids of the wearer, respectively, whereas the filter layer is used to prevent the transmission of virus-adsorbed and other aerosol particles. With the widespread use of surgical masks and their effectiveness against SARS-CoV-2, many relevant studies [8–14] have focused on the total filtration efficiency of surgical masks or research and development of filtration material.

Nazek et al. [15] have improved a nanoporous flexible Si-based template on a silicon-on-insulator (SOI) wafer utilizing potassium hydroxides (KOH) etching, utilizing the template as a hard mask through a reactive ion etching process for transferring patterns onto a lightweight ( $<0.12$  g) and flexible polymeric membrane. The flexible membrane might be utilized on the mask as reusable to boost its filtration efficiency against submicron particles, including COVID-19. Furthermore, mask reusability contributes toward eliminating the challenges surrounding single-use face mask shortages and reducing plastic pollution from disposable masks. However, research on the aerosol particle filtration mechanism of each layer of three-layer surgical masks is lacking. With no information related to filtration efficiency and resistance per layer of the currently available mask, the design and development of high-performance surgical masks may be difficult.

In recent decades, computational fluid dynamics (CFD) has been widely used to study the filtration performance of masks [16,17]. Through extensive research on fibrous media, researchers have greatly contributed to the development of filtration theory. When CFD is used for numerical simulation, fiber-particle interaction can be simulated using a single fiber model [17,18]. Several CFD techniques, including the Monte Carlo simulation technique, Lattice-Boltzmann method, and ANSYS-Fluent CFD code (CFD-DPM + UDF), have been used to effectively study the deposition and particle filtration processes of single fiber surfaces [19–21]. However, most of the relevant works have been limited by construction of single fiber models only. Recently, several studies have reported the construction of three-dimensional (3D) models of fibrous media [22,23]. Zhang et al. [22] established three arrangement types of fibrous media to investigate the effects of structural parameters on the filtration performance; the authors observed that the

arrangement type of the fibrous media significantly affected their filtration efficiency but not their pressure drop. Several researchers have used the CFD-DEM method as well as scanning electron microscopy (SEM) images to analyze the influence of different fiber structures and particle size on the pressure drop and filtration characteristics of 3D models of fibrous media [24–27]. These studies not only predicted the filtration performance of fibrous media but also observed the entire filtration process. Some researchers have also studied the filtration performance of fibrous media by using a numerical simulation method and a physical model structure. Gervais et al. [28] adopted image processing technology to establish 3D models of a fibrous medium and then simulated the filtration properties of fibrous media by using GeoDict. Moreover, Cao et al. [23] used the Voronoi algorithm to reconstruct the 3D modeling of a fibrous medium and then systematically conducted numerical simulations with flow characteristics. The results of the aforementioned studies aided in verifying the pressure drop and filtration efficiency of fibrous media under different fiber diameters, volume fractions, thicknesses, and velocities. Although WHO-certified surgical masks have a three-layer structure, studies on the contribution of each layer structure to the overall filtration capacity and air resistance, particularly using numerical simulations, are lacking. Therefore, the aforementioned research gap by constructing and using a 3D multiphase flow model was filled in the present study.

Aerosol particles can be filtered by mask fibers through four main mechanisms: interception, inertial impaction, Brownian diffusion, and gravitational settling [29]. Aerosol particle density plays a crucial role in all the four mechanisms [29,30]. Particulate matter density also determines the mixing, transport effects, and deposition of complex and dynamic atmospheric aerosols in the air and in the human respiratory system [31]. On the basis of a large number of measurement data, Rissler et al. [32] and Yin et al. [33] concluded that aerosol particle density in air varies with particle size. Therefore, the effects of aerosol particle density on filtration were studied in the present study.

Surgical masks operate on various filtration mechanisms to fulfil the requirements, which include direct interception, diffusion, inertial

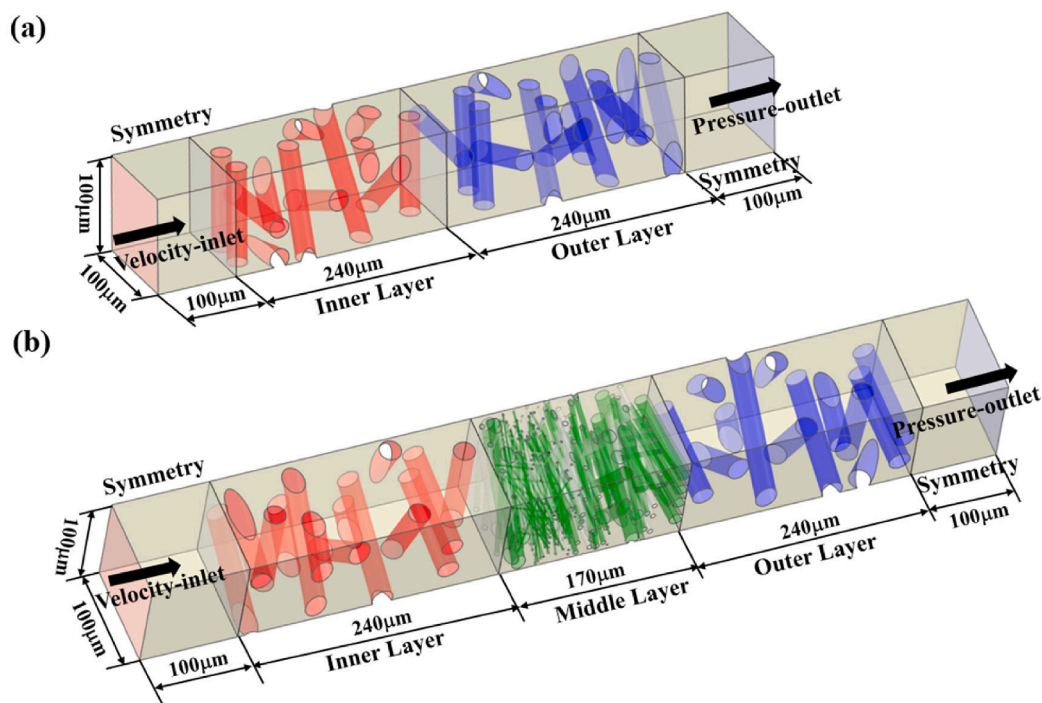


Fig. 2. Structure and boundary conditions of Models (a) I and (b) II.

impaction, and electrostatic interaction [34]. In areas with high humidity, under ultraviolet light towers, even large fumigants can eliminate static electricity in surgical masks. Based on this, the main objective of the current study was to experimentally and numerically reveal the particle size-dependent filtration mechanism (direct interception, diffusion and inertial impaction) of each layer of a three-layer surgical mask. Our comparative study may aid in quantifying the contribution of each layer to the filtration efficiency and respiratory resistance of a surgical mask. The remainder of this article is structured as follows: Section 2 describes models and mathematical theories related to the multiphase flow calculation used in this work. Section 3 mainly describes the experimental processes related to aerosol filtration efficiency and respiratory resistance measurements. In Section 4, the results of the comparative studies based on experimental measurements and numerical simulations are stated and discussed.

The representative 3D fiber models of two SEM-based morphology of surgical masks were established including fiber diameter, filter material thickness, and solid volume fraction (SVF): Model I, a mask composed of only two spun-bond polypropylene nonwoven fabric layers (without a filter layer), and Model II, a full mask model composed of two spun-bond polypropylene nonwoven fabric layers and one melt-blown nonwoven polypropylene fabric (with a filter layer). Model III with one layer of spun-bond polypropylene nonwoven fabric, and Model IV with one layer of melt-blown nonwoven polypropylene fabric were also established. It should be pointed out that in the experiment of this article, the mask has been in a dry state. Therefore, in the establishment of the mathematical model, the influence of the humidity of the mask on the filtration problem is not considered.

## 2. Mathematical models

### 2.1. 3D modeling of fibrous media

The 3D micro scale surgical mask models were constructed as follows: (1) Filed Emission Scanning Electron Microscopy (SEM, Zeiss Gemini 300) was conducted to obtain the microstructure and distribution of the inner and outer layers (spun-bond polypropylene nonwoven

Table 1

Physical properties of different filter media.

Filter material	Gram weight (g cm <sup>-2</sup> )	Thickness (μm)	Fiber diameter (μm)	SVF (%)
Spun-bond polypropylene nonwoven fabric	23	240	20	11.23
Melt-blown nonwoven polypropylene fabric	25	170	3.06 (2(58%)/5 (32%)/13 (10%))	41.53

fabrics) and middle layer (melt-blown nonwoven polypropylene fabric) of a surgical mask complying with People's Republic of China Pharmaceutical Industry Standard YY 0469–2011 (Fig. 1). (2) Fiber size as well as the thickness and SVF of the fibrous medium were measured. (3) According to the extracted structural parameters, the 3D models of fibrous media with a stochastic algorithm were established.

Only surgical masks from Zhende Medical, complying with People's Republic of China Pharmaceutical Industry Standard YY 0469–2011, were selected as research objects. Fig. 1 illustrates SEM images of the surfaces of the two types of fibrous media of the surgical mask. In both the media, fiber arrangement was irregular, and the shape and size of pores formed by the interlaced fibers were nonuniform. The fiber diameter of spun-bond polypropylene nonwoven fabric (Fig. 1(c) and 1(e)) was approximately 20 μm. The fiber diameter of melt-blown nonwoven polypropylene fabric (Fig. 2(d)) varied greatly; it was approximately 2, 5, and 13 μm in 58%, 32%, and 10% of the cases, respectively. Correspondingly, the statistical mean of fiber diameter is 3.06 μm. The thickness of spun-bond polypropylene nonwoven fabric and melt-blown nonwoven polypropylene fabric was approximately 240 and 170 μm, respectively (Fig. 1(f), 1(g) and 1(h)). The physical characteristics of the spun-bond and melt-blown nonwoven polypropylene fabrics are summarized in Table 1; their SVF was 11.23% and 41.53%, respectively.

As shown in Fig. 1, the fiber arrangement demonstrated a random distribution; thus, the fiber models were established using the random



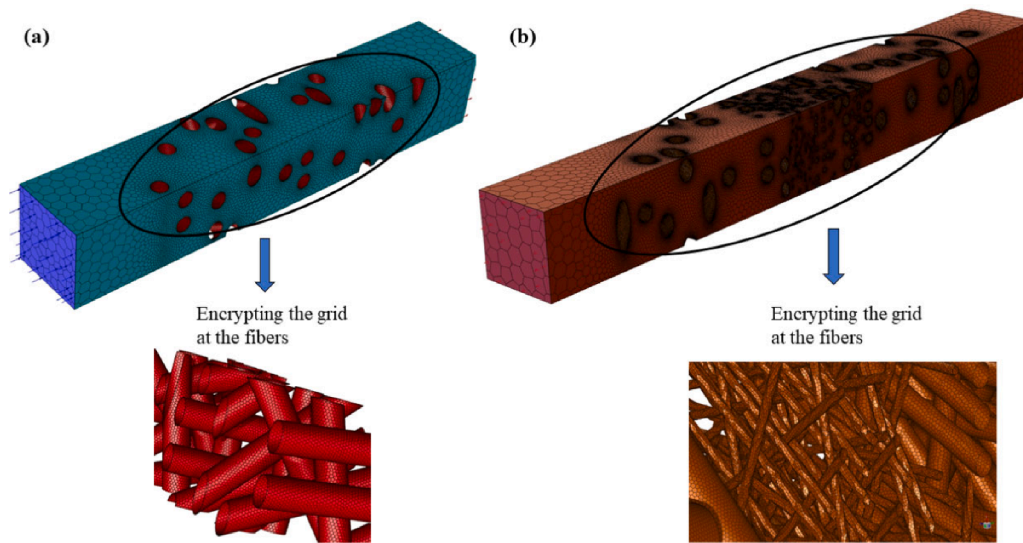


Fig. 3. Computational grids in Models (a) I and (b) II.

method. SolidWorks 2017 was used to establish cuboid computing domain and randomly generate two endpoints on four opposite surfaces of the cuboid area. According to the random endpoints, a cylinder was generated; here, cylinders represent fibers. The fibers, which did not cross each other, were then combined with the cuboid. Our 3D microscopic models of the fibrous media was finally established by deleting the fibers outside the cuboid area. Assumption was made that none of the fibers were bent. Next, two models were established according to the physical characteristics of Table 1: Model I, composed of the inner and outer spun-bond polypropylene nonwoven fabric layers, and Model II, a three-layer fiber model of the surgical mask. Here, Model I was used as a validation model for performing a comparative study and considered Model II as the real model of the commercial surgical mask. The established fibrous media were imported into Ansys-Space Clime to calibrate their SVF, as shown in Fig. 2.

## 2.2. Mathematical theory

### 2.2.1. Gas phase model

The Euler–Lagrangian method was previously used to investigate the flow of gas and solid phases in the fibrous media of a surgical mask [35]. In CFD calculations, gas is considered a continuous phase, and the finite volume method implemented in Fluent is used to solve the flow field through continuity equation of local mean variable and momentum conservation (N-S) equation [26,35]:

$$\frac{\partial}{\partial t}(\epsilon\rho) + \nabla \cdot (\epsilon\rho\mathbf{u}) = 0 \quad (1)$$

$$\frac{\partial}{\partial t}(\epsilon\rho\mathbf{u}) + \nabla \cdot (\epsilon\rho\mathbf{u}\mathbf{u}) = -\epsilon\nabla p + \nabla \cdot (\epsilon\tau) + \rho\epsilon\mathbf{g} + \mathbf{F} \quad (2)$$

where  $\mathbf{F}$  represents the interaction force between the particle and the fluid:

$$\mathbf{F} = \sum_{i=1}^n \frac{\mathbf{f}_{d,i}}{\Delta V} \quad (3)$$

where  $\mathbf{f}_{d,i}$  is the resistance exerted on the particle  $i$ ,  $\Delta V$  is the volume of the computing unit,  $n$  is the number of particles in the computing unit.

The gas-phase stress tensor in CFD can be represented by  $\tau$ :

$$\tau = \epsilon\mu(\nabla\mathbf{u} + \nabla\mathbf{u}^T) - \frac{2}{3}\nabla \cdot \mathbf{u}\mathbf{I} \quad (4)$$

where  $\epsilon$  is the volume fraction of the gas phase,  $\rho$  is the density of the gas phase,  $\mathbf{u}$  is the velocity vector of the gas phase,  $p$  is the pressure of the gas phase,  $\mathbf{g}$  is the gravitational acceleration constant,  $\mu$  is the viscosity of the fluid, and  $\mathbf{I}$  is a unit tensor.

A fluid may demonstrate laminar or turbulent flow. Whether the flow is laminar or turbulent depends on whether its Reynolds number ( $Re$ ) exceeds the critical Reynolds number.  $Re$  is defined as follows:

$$Re = \frac{\rho u L}{\mu} \quad (5)$$

where  $\rho$  is the density of the fluid,  $u$  is the flow velocity of the fluid,  $L$  is the characteristic length, and  $\mu$  is the dynamic viscosity of the fluid.

In the present study, the fiber diameter was small, with a gas velocity of  $0.064\text{--}0.272\text{ m s}^{-1}$ ; therefore, the calculated  $Re$  was much lower than 1. Therefore, gas flow through the fibrous media of a surgical mask is laminar.

### 2.2.2. Solid phase model

The particle–fiber and particle–particle interactions during filtration can be solved according to the equations for Newton's second law translation and rotation [26]:

$$m_{p,i} \frac{d\mathbf{u}_{p,i}}{dt} = m_{p,i}\mathbf{g} + \mathbf{f}_{f,i} + \mathbf{f}_{c,i} \quad (6)$$

$$I_{p,i} \frac{d\boldsymbol{\omega}_{p,i}}{dt} = \sum \mathbf{T}_i \quad (7)$$

where  $m_{p,i}$  is the mass of the particle  $i$ ,  $\mathbf{u}_{p,i}$  is the translation vector of the particle  $i$ ,  $\boldsymbol{\omega}_{p,i}$  is the angular velocity vector of the particle  $i$ ,  $\mathbf{f}_{f,i}$  is the applied particle  $i$ ,  $\mathbf{f}_{c,i}$  is the collision force between particles,  $I_{p,i}$  is the moment of inertia of the particle  $i$ , and  $\sum \mathbf{T}_i$  is the vector sum of the collision moment.

In the computational domain, when particles collide with particles or fibers, the collision and capture of particles can be judged according to the position and velocity of the particles. If the distance between the particle and fiber surface is less than the radius of the particle, then the particle and the fiber will collide. If the velocity of the particle changes to zero, then the particle will be captured by the fiber and deposits will form on the fiber surface [36]. The particle velocity and position in the simulation domain can be obtained by integrating the balance of forces acting on the particle through Lagrangian tracking [27].

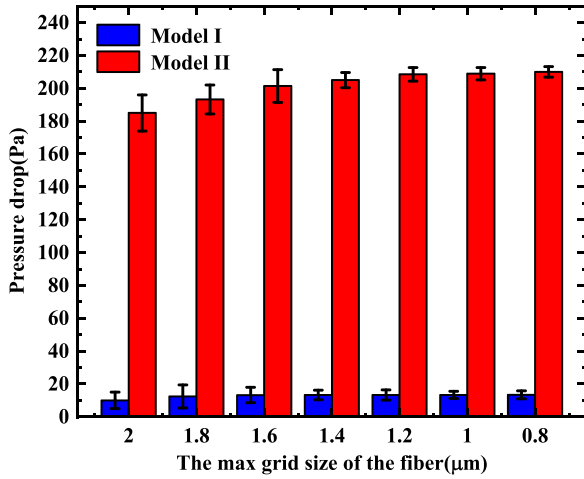


Fig. 4. The effect of max grid size at the fiber on pressure drop.

$$\frac{dV_p}{dt} = \frac{18\mu}{d_p^2 \rho_p C_c} (V - V_p) \quad (8)$$

where  $V_p$  is the velocity of the particle  $p$ ,  $C_c$  is the Cunningham correction factor,  $\mu$  is the fluid viscosity, and  $\rho_p$  is the density of the particle  $p$  [37].

For submicron particles, Saffman's lift force ( $F_{sl}$ ) and Brownian force ( $F_{bi}$ ) should be considered [38,39]. The expressions of  $F_{sl}$  and  $F_{bi}$  are as follows:

$$F_{sl} = \frac{2Kv^{\frac{1}{2}}\rho d_{ij}}{\rho_p d_p (d_{ik} d_{kl})^{\frac{1}{2}}} (u - u_p) \quad (9)$$

$$F_{bi} = \zeta_i \sqrt{\frac{\pi S_o}{\Delta t}} \quad (10)$$

$$S_o = \frac{S_{n,ij}}{\delta_{ij}} = \frac{216\nu\sigma T}{\pi^2 \rho d_p^5 (\frac{\rho_p}{\rho}) C_c} \quad (11)$$

where  $K = 2.594$ ,  $d_{ij}$  is the deformation tensor,  $S_{n,ij}$  is the spectral intensity,  $\delta_{ij}$  is the Kronecker function,  $\nu$  is the kinematic viscosity,  $\sigma$  is the Boltzmann constant,  $\zeta_i$  is a Gaussian random number, and  $\Delta t$  is the time in the numerical simulation step.

### 2.3. Numerical simulation

As shown in Fig. 1, the fiber arrangement in the mask was random; therefore, generating hexahedral meshes for numerical simulation became difficult to achieve. Thus, polyhedral meshes were divided in the two fiber models, as shown in Fig. 3. Before drawing any conclusions from the numerical results, we should ensure that the numerical results are not mesh dependent. In order to verify the independence of numerical results from the number of grids, the relationship between the pressure drop of the two fiber models and the max grid size at the fiber is shown in Fig. 4. It can be seen that with the decrease of max grid size of the fiber, the pressure drop gradually increases and finally stabilizes.

The Model I grid is displayed in Fig. 3(a). Here, the maximum mesh length was  $9.375 \times 10^{-6}$  m, the minimum volume mesh size was  $5.8594 \times 10^{-7}$  m, and the total number of mesh units was 371,620. The Model II grid is presented in Fig. 3(b). Here, the maximum mesh size was  $6.6406 \times 10^{-6}$  m, the minimum volume mesh size was  $8.3007 \times 10^{-7}$  m, and the total number of mesh units was 3,647,944.

The computational domain and boundary conditions of the numerical simulation of Models I and II are presented in Fig. 2(a) and 2(b), respectively. For the continuous phase, the flow entered the computational domain through the left velocity inlet and left the computational

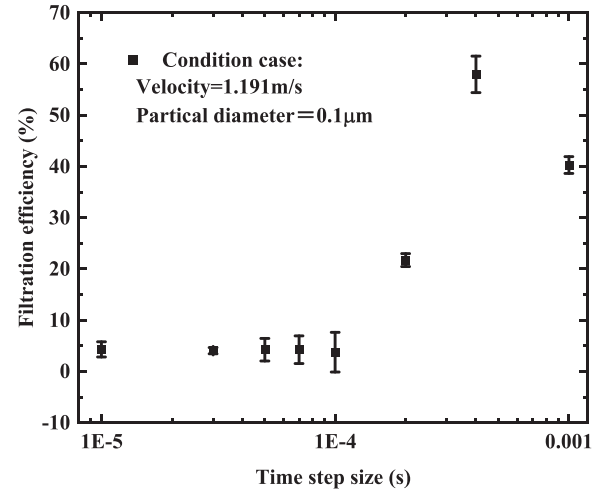


Fig. 5. Effects of time step on filtration efficiency in numerical simulation (Model I).

domain through the right pressure outlet. When the initial inlet velocity is given, the velocity in the fluid is 0. The remaining four faces of the computational domain were set as symmetrical boundary conditions, and the boundary conditions of the filaments in the fluid domain were set as the wall boundaries. It is worth noting that the fibrous media in the simulation area is taken from the overall fibrous filter, and there is no significant lateral airflow. Hence, the treatment of the computational sides with symmetry boundary does not affect the simulation results [23]. In the inner and outer layers of Models I and II, the distance between the outlet and front of the fibrous media and the distance between the outlet and end of the fibrous media were both 100 μm. The computational domains of Models I and II were  $100 \mu\text{m} \times 100 \mu\text{m} \times 680 \mu\text{m}$  and  $100 \mu\text{m} \times 100 \mu\text{m} \times 850 \mu\text{m}$ , respectively. After the boundary conditions were set, the flow field could be calculated. When the residual convergent errors of the continuity equation and the momentum equation in all directions were less than and the average velocity fluctuation at the outlet was  $< 5\%$ , the flow field tended to be in a stable state. After flow field calculations were completed, we injected nine sets of particles varying in size continuously from the entrance. For each computational case, the number of particles released from the inlet boundary was 1000, and the calculations were performed three times. The average of these three calculations was considered the final result. The boundary condition of the fiber was set to trap, whereas that of the outlet was set to escape. The residuals at each time step were required to be below the convergence residual criterion for transient computations during the simulation [40]. For the universality of the research, we selected the particle system in the range of 0.1–2 μm for research. Here it is necessary to point out that our numerical model is equally valid for particle systems smaller than 0.1 μm.

In the present study, the computational time step was specified by evaluating the interception efficiency of particles. The interception efficiency of particles was calculated from the changes in particle number at the outlet and inlet:

$$\eta = \frac{N_{in} - N_{out}}{N_{in}} \times 100\% \quad (12)$$

where  $N_{in}$  represents the number of particles at the inlet and  $N_{out}$  represents the number of particles at the outlet. In the present study, the particles were sprayed from the inlet; thereafter, some particles flowing through the fibers became trapped, whereas the uncaptured particles escaped from the outlet. The filtration efficiency of the particles was calculated on the basis of the numbers of injected  $N_{in}$  and escaped particles  $N_{out}$ .

As shown in Fig. 5, the effects of the time step on filtration efficiency

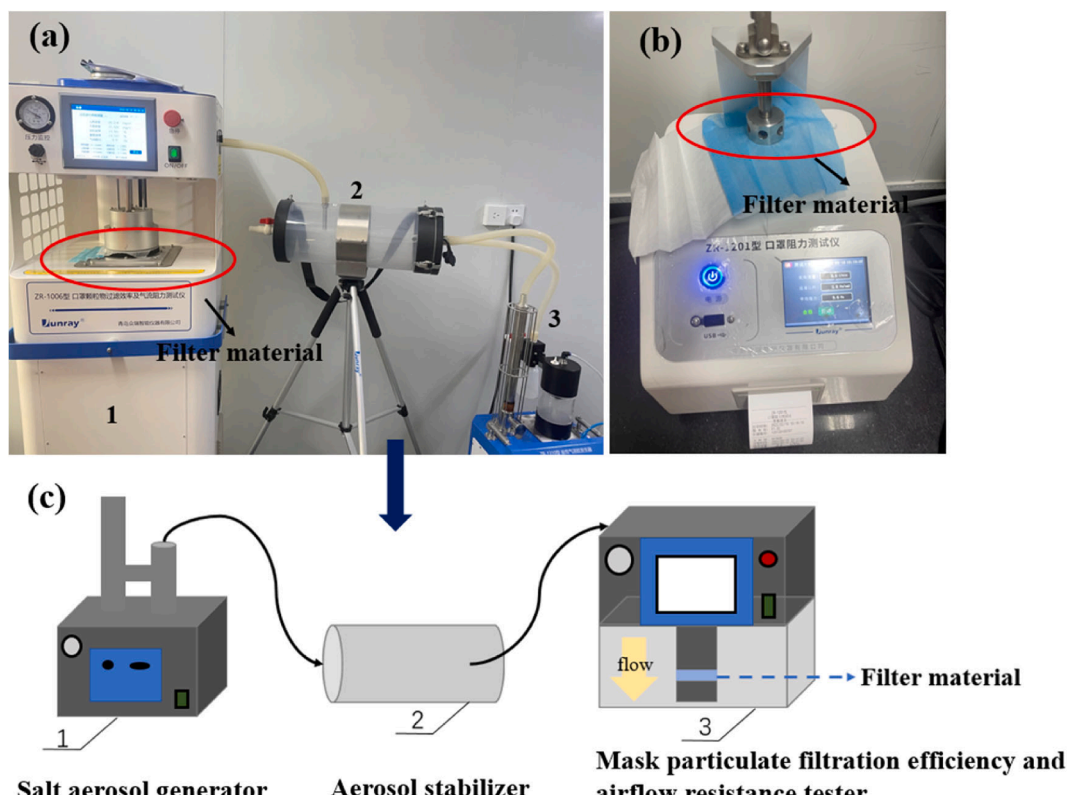


Fig. 6. Experimental platforms: (a) filtration efficiency bench, (b) pressure drop test bench and (c) schematic of filtration efficiency test bench.

during the numerical simulation was compared. For instance, in Model I, when the time step was lower than  $1.0\text{E-}4$ , filtration efficiency tended to be stable. Hence,  $1.0\text{E-}5$  was selected as the time step in the simulation for reliability.

### 3. Experimental section

#### 3.1. SEM observation

The SEM images of spun-bond and melt-blown nonwoven polypropylene fabrics in our surgical mask as well as their cross-section morphology are presented in Fig. 1. Each fibrous medium was cut to an appropriate size by using a blade and held onto the sample table by using a conductive carbon glue. To improve the electrical conductivity of the fibrous media, the Em Ace200 (Leica) gold-plating equipment was used to spray gold for 45 s on their surfaces; moreover, the test voltage was set at 2 kV.

#### 3.2. Experimental platform

The experimental platform (Fig. 6) was set up according to ASTM F2100-2018/DIN EN 14683, which was used to measure the total filtration efficiency and pressure drop of the filter media. A schematic of the experimental setup for the detection of fiber materials' filtration efficiency is presented in Fig. 6(c). Here, total filtration efficiency was measured using a respirator particle filtration efficiency and airflow resistance tester (ZR-1006; Qingdao Zhongrui, China), an aerosol stabilizer, and a salt aerosol generator. A 1.5% NaCl solution was atomized using a collision nozzle to generate particles in the range of  $0.02\text{--}2\text{ }\mu\text{m}$  in diameter. Pressure drop was determined using a resistance tester (ZR-1201; Qingdao Zhongrui).

#### 3.3. Experimental process

In accordance with DIN EN 14683 and YY 0469-2011,  $100\text{ cm}^2$  was used as the test area to assess surgical mask filtration efficiency at  $0.064\text{ m s}^{-1}$ . The filtration efficiency and pressure drop in Models IV (i.e., melt-blown nonwoven polypropylene fabric in the middle layer), I, and II were measured using velocity of  $0.064$ ,  $0.127$ ,  $0.191$ , and  $0.255\text{ m s}^{-1}$ . Multiple filter media from the same production batches were selected as experimental samples to reduce the possibility of errors. The filtration efficiency of the filter media was calculated using Eq. (12).

The breathing resistance of the filter media was calculated on the basis of the pressure upstream and downstream of the filter media,  $4.9\text{ cm}^2$  was used as the test area to assess surgical mask filtration efficiency at  $8\text{ L min}^{-1}$  (DIN EN 14683/YY 0469-2011): The value of the pressure difference per square centimetre of area is shown in Eq. (13):

$$\Delta P = \frac{P_M}{4.9} \quad (13)$$

where  $P_M$  is the average value of the test sample pressure difference.

### 4. Results and discussion

#### 4.1. Verification of numerical simulation by evaluating respiratory resistance

The numerical simulation results were verified for respiratory resistance of the surgical mask layers by comparing them with those of other works. Resistance is the pressure difference between inlet and outlet of a filter; it is a crucial parameter reflect filter performance. The linear fitting between filtration velocity and pressure drop of Models I and II is displayed in Fig. 7(a) and 7(b), respectively. The correlation between pressure drop and velocity was found to be positive [41,42].

According to Darcy's law, the resistance of fibrous media is generally expressed as a function of dimensionless resistance [43]:

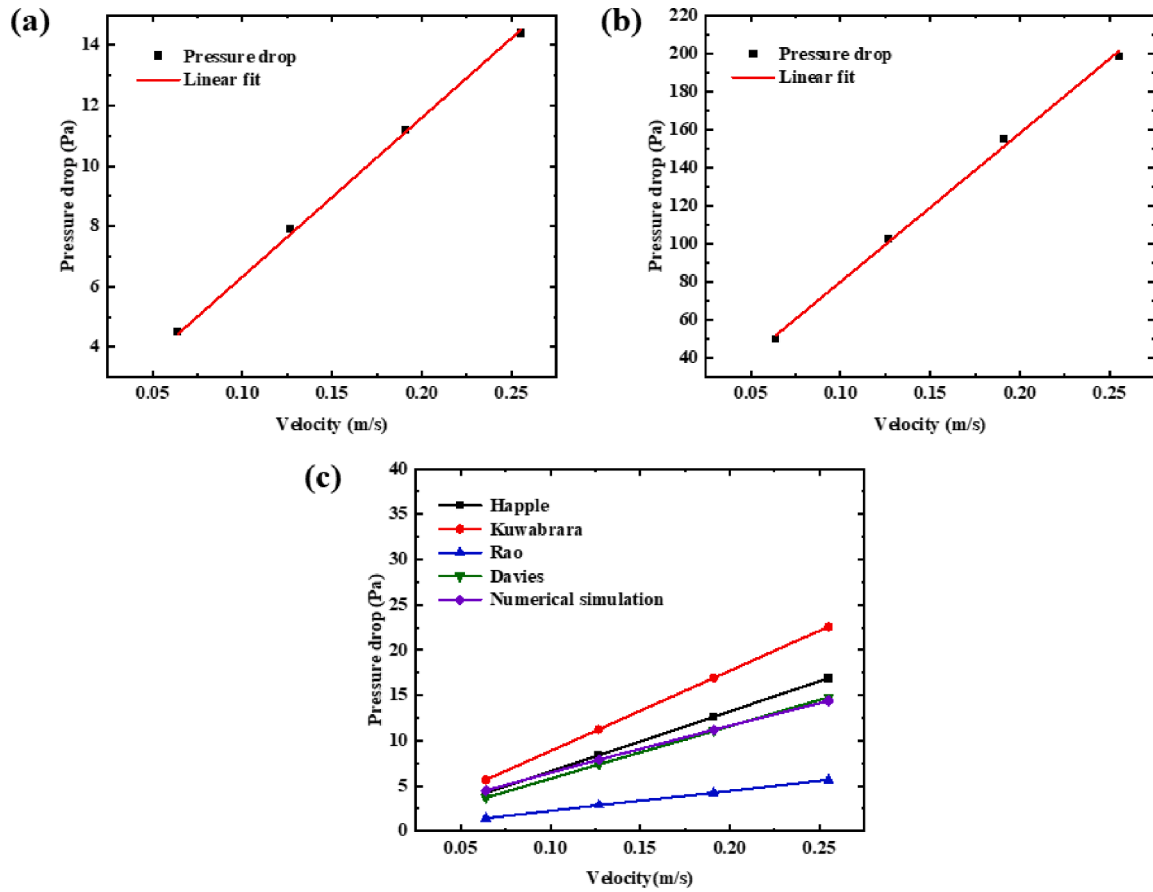


Fig. 7. Fitting line of filtration velocity and pressure drop under Models (a) I and (b) II and comparison between numerical and empirical fibrous medium resistance at different velocities in Model I of (c).

$$\Delta P = \frac{V\eta h}{d_f^2} f(\alpha) \quad (14)$$

where  $\eta$  is the dynamic viscosity of fluid,  $h$  is the thickness of filter material,  $d_f$  is fiber diameter, and  $f(\alpha)$  is the dimensionless resistance, which is only a function of the filling density  $\alpha$ .

Happel [44] and Kuwabara [45] hypothesized that the shear stress on the fiber surface was 0 and provided the following dimensionless resistance expression:

$$f(\alpha) = \frac{16\alpha}{-0.5\ln\alpha - 0.5\frac{1-\alpha^2}{1+\alpha^2}} \quad (15)$$

$$f(\alpha) = \frac{16\alpha}{-0.5\ln\alpha + \alpha - \frac{3}{4} - \frac{\alpha^2}{4}} \quad (16)$$

Davies [46] and Rao [47] studied the pressure drop of the fibrous media through experimentation and numerical simulation, respectively. The dimensionless pressure drop based on their work can be expressed as [23]

$$f(\alpha) = 64\alpha^3(1 + 56\alpha^3) \quad (17)$$

$$f(\alpha) = 2.653\alpha + 39.34\alpha^2 + 144.5\alpha^3 \quad (18)$$

The numerical results for resistance in Model I, based on the CFD calculations in Section 2.2 and values from previous studies at different velocities, are presented in Fig. 7(c). The pressure drop calculated based on the present numerical simulation was in good agreement with the pressure drop calculated using the Davies experimental correlation formula, and the maximum error was  $< 2\%$ . The prediction effect of Happel unit model is close to the Davies experimental correlation

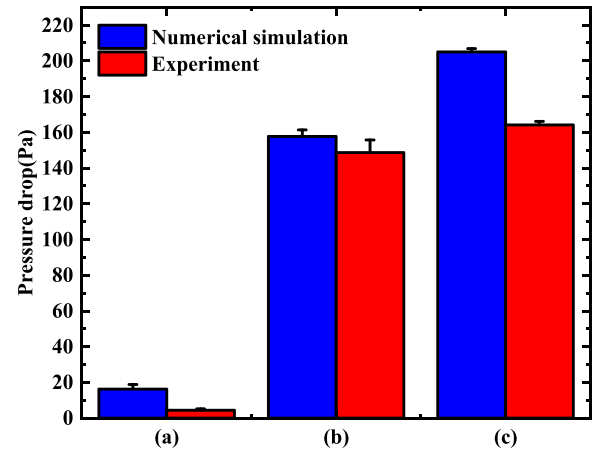


Fig. 8. Comparison of simulated and measured pressure drop in three cases at a flow rate of  $8 \text{ L min}^{-1}$  in Models (a) III, (b) IV, and (c) II.

formula, the prediction value of Kuwabara unit model is much higher than the experimental value, and the prediction value of Rao unit model is much lower than the experimental value [44–47]. Therefore, from the above comparison results, it can be seen that the numerical calculation model in this paper can be used to predict the pressure loss of fiber filter media.

The pressure drops in Models III, IV, and II were measured using the resistance tester ZR-1201. As shown in Fig. 8, the pressure drop noted in the CFD calculations was used for a comparative study. The numerical simulation results were close to the experimental results in all the three



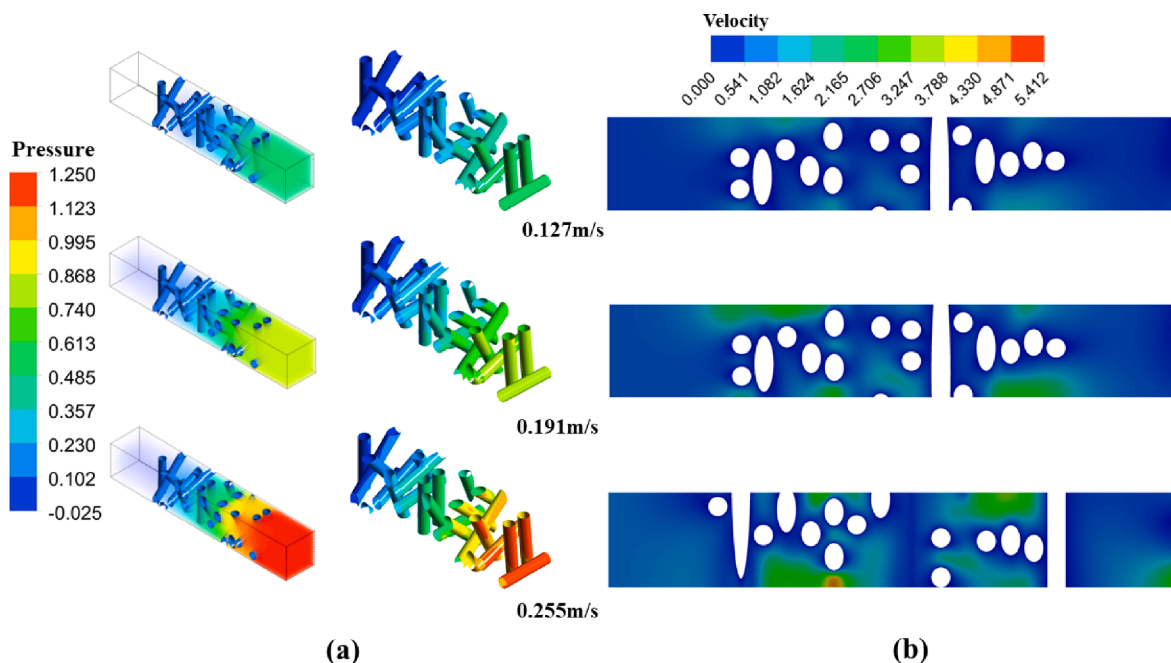


Fig. 9. Internal flow field in Model I at different velocities.

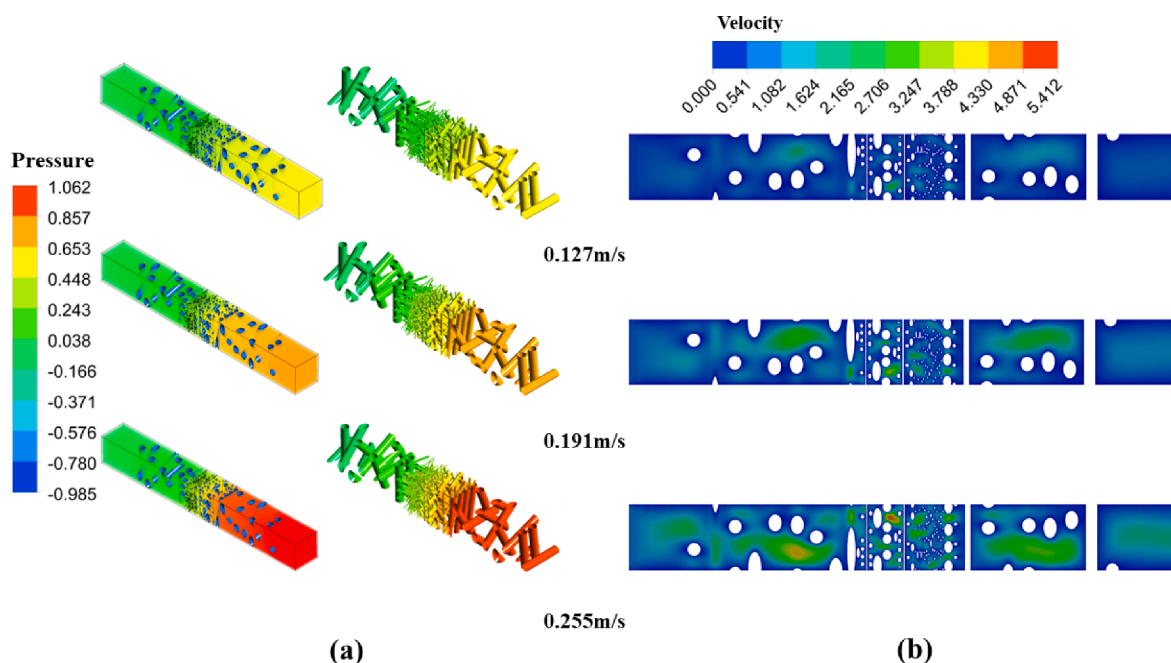


Fig. 10. Internal flow field in Model II at different velocities.

models. In the experimental results, the pressure drop in Model III (4.4 Pa) was much lower than that in Model IV (148.7 Pa). The difference between the pressure drop in Models III and IV was  $> 97\%$ . Model IV demonstrated a slightly lower pressure drop than did Model II, with a difference of only approximately 10%. These results indicated that the main respiratory resistance of the surgical mask originated from the middle melt-blown fabric layer, which contributed to  $> 90\%$  resistance. As shown in Fig. 8, the measured pressure drop in Models IV and II was 148.7 and 164.15 Pa, respectively—consistent with the measured data of Podgórski et al. and Hassan et al. [48,49], where the pressure drop of melt-blown fabrics was 173 and 270 Pa, respectively.

#### 4.2. Internal flow field distribution

In the process of filtration by fibrous media, the fundamental factor affecting resistance is fluid flow between pores. This feature was well-reflected in our fibrous medium models. The internal flow fields with different filtration velocities (0.127, 0.191, and  $0.255 \text{ m s}^{-1}$ ) in Models I and II are presented in Figs. 9 and 10, respectively. For a better presentation of the results, dimensionless pressure and speed are applied to use the full range of colour bars ( $P/P_{\text{max}}$  and  $V/V_{\text{max}}$ ).

Wherein, the pressure drop of Model I and Model II at  $0.255 \text{ m s}^{-1}$  was selected as  $P_{\text{max}}$  of Model I (14.98 Pa) and Model II (200.04 Pa), respectively, and the maximum inlet velocity of  $0.255 \text{ m s}^{-1}$  was

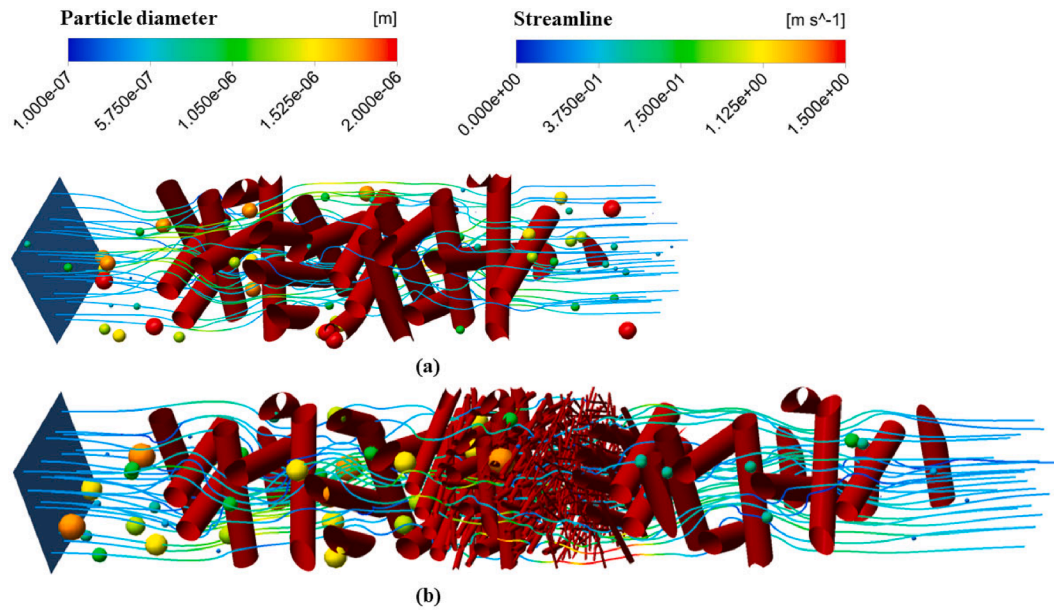


Fig. 11. Filtration process and movement track of particles in Models (a) I and (b) II.

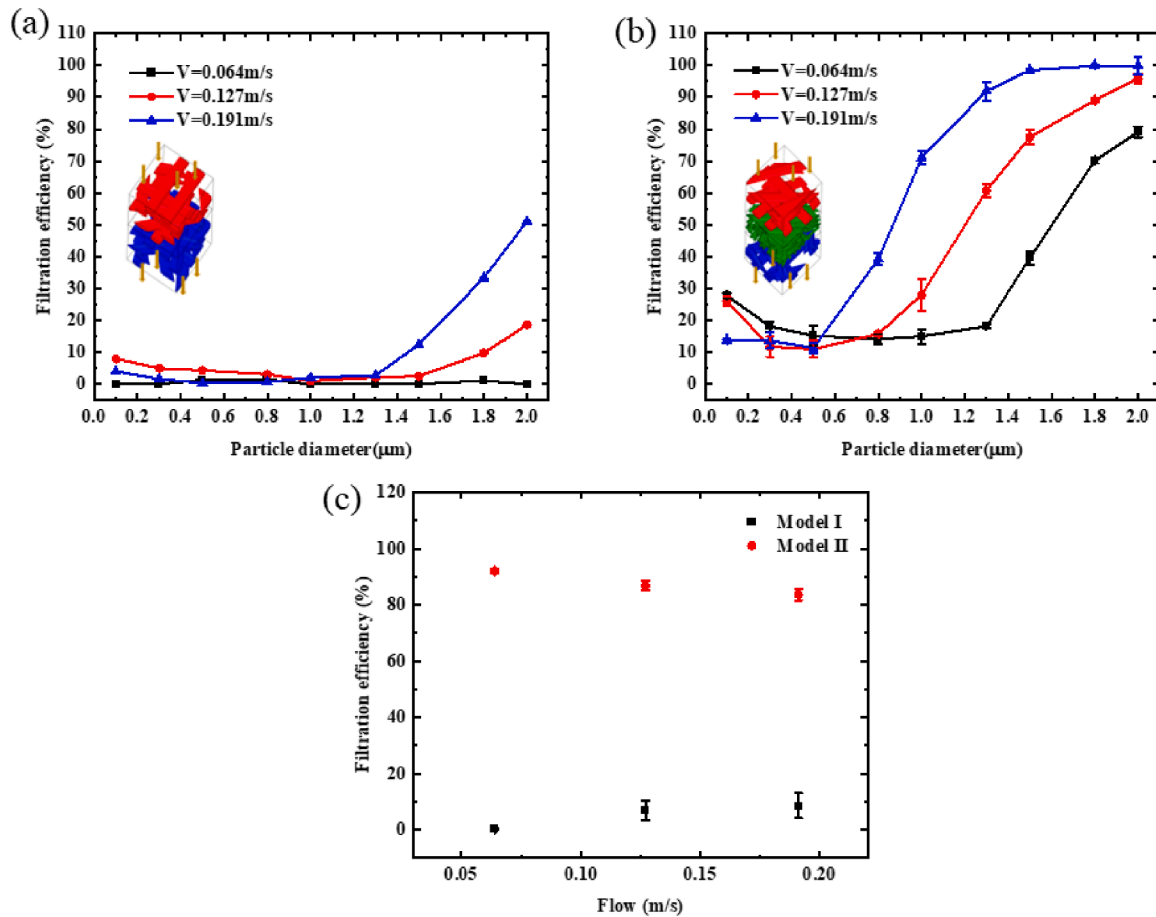


Fig. 12. Filtration efficiency at different velocities in Models: (a) numerical simulation of Model I, (b) numerical simulation of Model II, (c) experiment.

selected as  $V_{\max}$  of Model I and Model II. Based on the pressure distribution, shown in Fig. 9(a) and 10(a), different inflow velocities led to a significant alteration in flow field and pressure differences. The number of vortices and velocity gradient near the fiber increased with an increase in velocity, as presented in the velocity contours of axially

symmetric sections in Fig. 9(b) and 10(b). At the same velocity, the pressure and velocity gradients and eddy current numbers were significantly higher in Model II than in Model I. This is because Model II had the middle melt-blown nonwoven polypropylene fabric filter layer in the surgical mask, and the SVF of this fabric is relatively high; consequently,

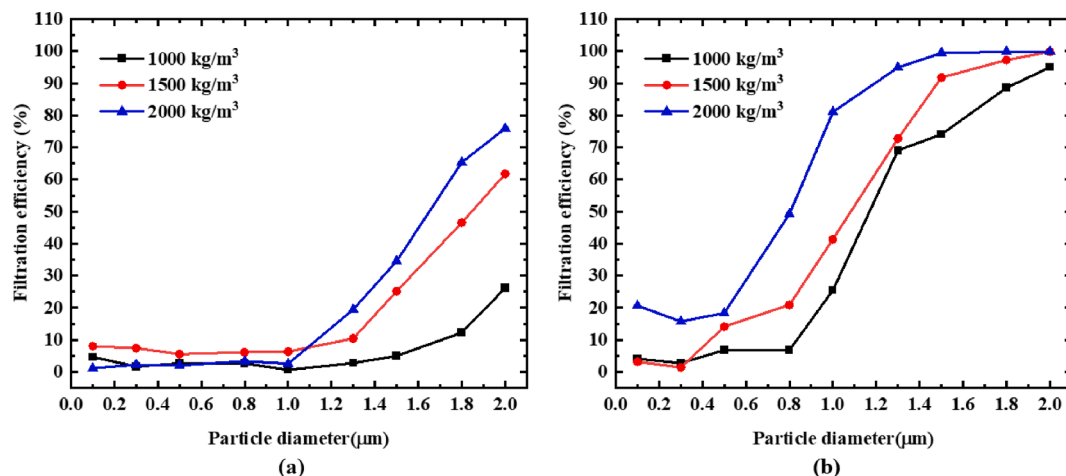


Fig. 13. Size-dependent filtration efficiency with different particle densities in Models (a) I and (b) II.

the SVF of the entire mask in Model I was relatively high. This phenomenon was also observed in the Voronoi-based microstructure model [23].

#### 4.3. Filtration efficiency

In the computational domains of two fibrous media, nine particle types in terms of particle diameters—namely 0.1, 0.3, 0.5, 0.8, 1.0, 1.3, 1.5, 1.8, and 2  $\mu\text{m}$ —were injected into flow from inlet at  $0.225 \text{ m s}^{-1}$ . During the filtration process of the fibrous media, on coming in contact with the fibers, the particles became stuck to the fibers to form dendrites on the fiber surfaces. The following particles were also observed to be captured and deposited to form dendrites. As particle deposition increased, the formed dendrites collapsed; this was followed by rebuilding of the dendrites. Model I (Fig. 11(a)) demonstrated low filtration efficiency and inability to effectively intercept almost submicron particles. However, in Model II (Fig. 11(b)), large micron-sized particles were effectively intercepted, and some submicron particles escaped through the outlet by bypassing the fibers. Because of the relatively large fiber spacing in Model I, the large-sized particles could bypass the fibers and escape through the outlet, indicating that the nonwoven fabric could not intercept the particles effectively and only absorbed human body fluids. Many particles were captured by the middle filter layer, and only a few particles passed through this layer and escaped through the outlet [40].

Fig. 12(a) and 12(b) present the overall statistical relationship filtration efficiency with particle diameter under different velocities in the simulated Models I and II, respectively. Model I demonstrated a considerably lower filtration efficiency than did Model II in the particle size range of 0.1–2.0  $\mu\text{m}$ . Model I could not capture submicron particles ( $\leq 1.0 \mu\text{m}$  in diameter) effectively. In most cases, Model I intercepted  $< 5\%$  of the aerosol particles. For relatively large particles with a diameter of 2.0  $\mu\text{m}$ , only Model I demonstrated the maximum filtration efficiency ( $\sim 50\%$ ) at maximum inflow velocity ( $0.191 \text{ m s}^{-1}$ ); however, under the same inflow velocity and particle diameter, Model II demonstrated the maximum filtration efficiency ( $\sim 100\%$ ). This is because compared with Model I, the added intermediate layer filter in Model II increased the thickness of the fibrous media and the SVF of the surgical mask, which greatly reduced the escape rate of particles. As shown in Fig. 12(b), Model II achieved the lowest filtration efficiency ( $\sim 15\%$ ) for particles with diameters of approximately 0.3  $\mu\text{m}$ . This finding is consistent with that reported previously [50–52]: the most-penetrating particle size of a traditional filter was observed to be approximately 0.3  $\mu\text{m}$ . Thus, existence of both the non-woven fabric layers for mechanical filtration and insertion of melt-blown fabric layer(s) in the face masks were found to be highly critical to prevent the airborne pathogen transmission [53,54].

Podgórski et al. observed that the filtration efficiency was the lowest for particles 10–500 nm in diameter [49]. This is because the main mechanism underlying the filtration of particles  $> 1 \mu\text{m}$  in diameter is inertial impaction, whereas the mechanisms underlying the filtration of particles  $< 0.3 \mu\text{m}$  in diameter are electrostatic force and Brownian diffusion.

As shown in Fig. 12(a) and 12(b), for particles  $> 1.0 \mu\text{m}$  in diameter, an increase in particle size led to increases in filtration efficiency. For particles  $< 0.3 \mu\text{m}$  in diameter, filtration efficiency decreased as the particle size increased. Filtration efficiency curves as a function of particle size, shown in Fig. 12(b), demonstrated a U-shaped distribution. Yue et al. [26] and Cao et al. [23] demonstrated similar results for the filtration process through fibrous media. The U-shaped distribution Fig. 12(a) is as not clear as that in Fig. 12(b). In Fig. 12(a), filtration efficiency remained constant initially; then, it gradually increased with increases in particle size. Moreover, based on the results in Fig. 12, for particles with a diameter of 2.0  $\mu\text{m}$ , Model II demonstrated filtration efficiencies of approximately  $\leq 2\%$ ,  $\leq 18\%$ , and  $\leq 50\%$  at velocities of 0.064, 0.127, and  $0.191 \text{ m s}^{-1}$ , respectively.

The comparison of the filtration efficiency between the numerical simulation and the experiment for the two fabric models was shown in Fig. 12(c). The trend of the numerical simulation value was basically consistent with the experimental test value. The data results were in good agreement with the deviation within 20% in Model I, which verified the feasibility of the numerical method. The velocity in the surgical mask model was positively correlated with the filtration efficiency, while the velocity in the experimental results was negatively correlated with the filtration efficiency. Besides, the numerical simulation value was slightly higher than the experimental value. The large deviation maybe has two reasons: Firstly, the surface of fiber media is not ideal smooth in the real state, and the fiber structure of melt-blown fabric in surgical masks are complicated, which affects the accuracy of SVF calculation. Secondly, when calculating the total filtration efficiency of numerical simulation, only nine different particle sizes was considered, which was not totally consistent with the fractional particle sizes in the experiment. Despite it is different between numerical simulation and experiment, our microscopic model will help predict the fractional filtration efficiency of masks, also be used to establish porous media model and broaden the way to study the filtration performance of fiber media [55].

Particle density, a physical quantity directly related to particle inertia, affects the particle inertia impaction mechanism. In the present study, the particle density was set at 1000, 1500, or  $2000 \text{ kg m}^{-3}$ . The filtration efficiency noted from simulation under different particle densities is displayed in Fig. 13. As shown in Fig. 13(a), the filtration efficiency for larger particles ( $> 1.0 \mu\text{m}$  in diameter) increased considerably with an increase in particle density, whereas that for smaller

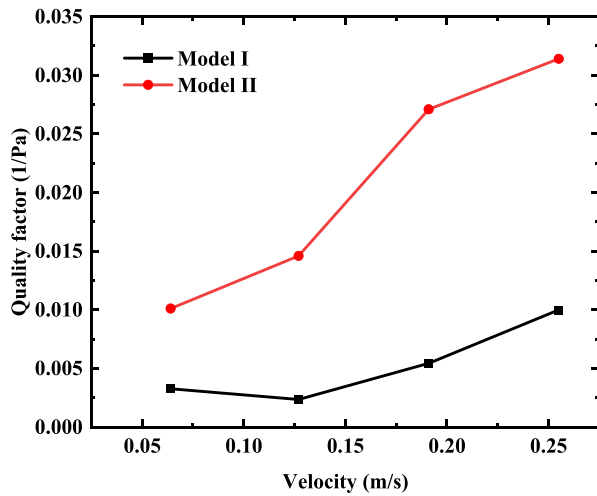


Fig. 14. Quality factor variation with the filtration velocity.

particles ( $<1.0 \mu\text{m}$  in diameter) did not demonstrate any such relationship. As shown in Fig. 13(b), the filtration efficiency for particles  $> 0.3 \mu\text{m}$  in diameter increased considerably with an increase in particle density. Therefore, particle density affected filtration efficiency only in the case of larger particles, this phenomenon is consistent with the research conclusion of Ying Sheng et al. [10]. When the particle density was high, the probability of inertial collisions of particle-particle or particle-fiber was high that was conducive for particles captured. In particular, the difference was more obvious in Model II than in Model I.

#### 4.4. Quality factor

The quality of filtration media is typically characterized by the quality factor, which is termed Alpha in the industry and is calculated by Eq. (19) [56,57]:

$$Q_F = -\frac{\ln(1-\eta)}{\Delta P} \quad (19)$$

where  $Q_F$  is the quality factor,  $\eta$  is the filtration efficiency.

As shown in Fig. 14, with an increase of velocity, the quality factors of the two fiber models showed different characteristics. For the inner and outer layer non-woven fabric model, when the filtration speed was  $>0.127 \text{ m s}^{-1}$ , the quality factor increased with the increase of the speed. For surgical mask model, when the filtration rate was in the range of  $0.064 \sim 0.225 \text{ m s}^{-1}$ , the quality factor with higher speed was higher. Human breathing, talking and coughing all spread viruses with particles into the air and wearing a mask can effectively intercept exhaled aerosols. The research of Soon-Park Kwon et al. [58] indicated that the average initial coughing velocity was  $15.3 \text{ m s}^{-1}$  for the males and  $10.6 \text{ m s}^{-1}$  for the females and the flow rate in the steady breathing state is much lower than in coughing, which indicating better filtration performance at high flow rates such as coughing. In addition, the quality factor of surgical mask model was much higher than that of inner and outer layers of non-woven fabric model. The calculation of  $Q_F$  can lead to a comprehensive and distinct understanding of fibrous structure and filtration properties [57,59].

#### 5. Conclusion

Three-layer surgical masks have become one of the important means for people to protect against SARS-CoV-2 virus infection. However, very little research on the filtering mechanism of three-layer surgical masks

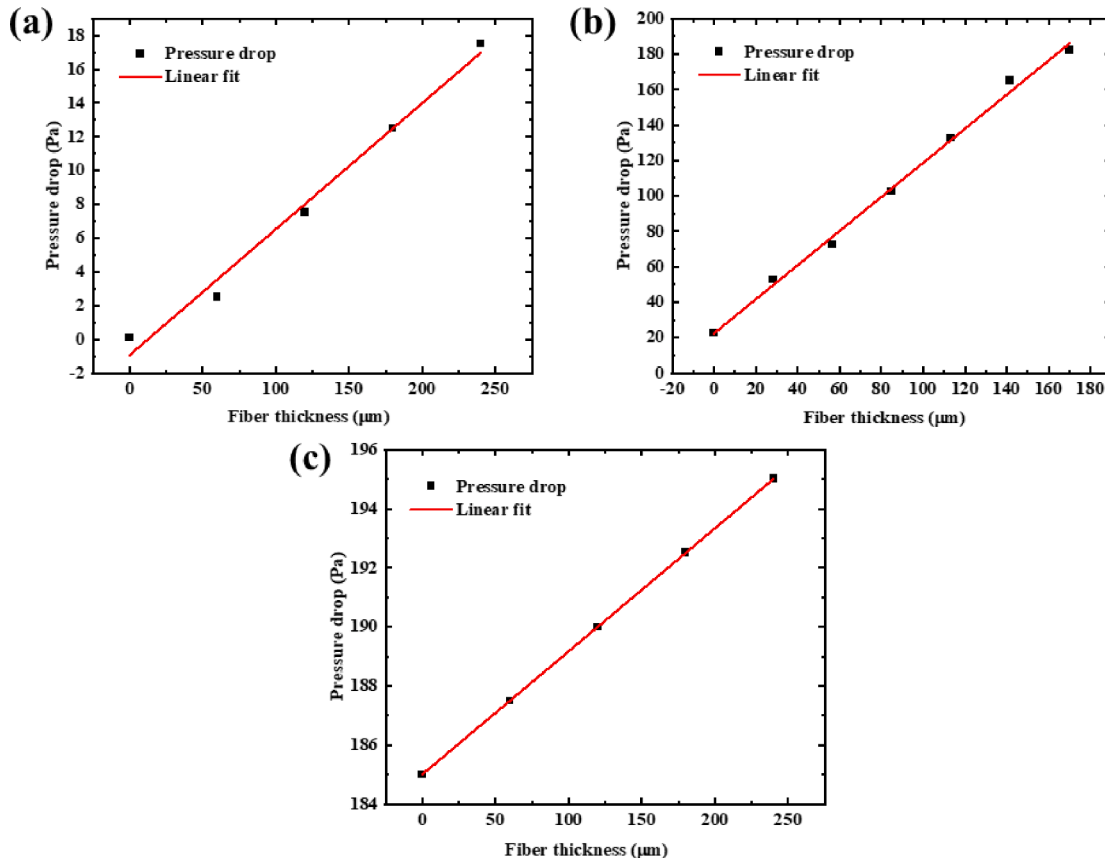


Fig. A1. Linear pressure drop distribution for each layer of fiber medium in Model II: (a) inner layer, (b) middle layer, (c) outer layer.



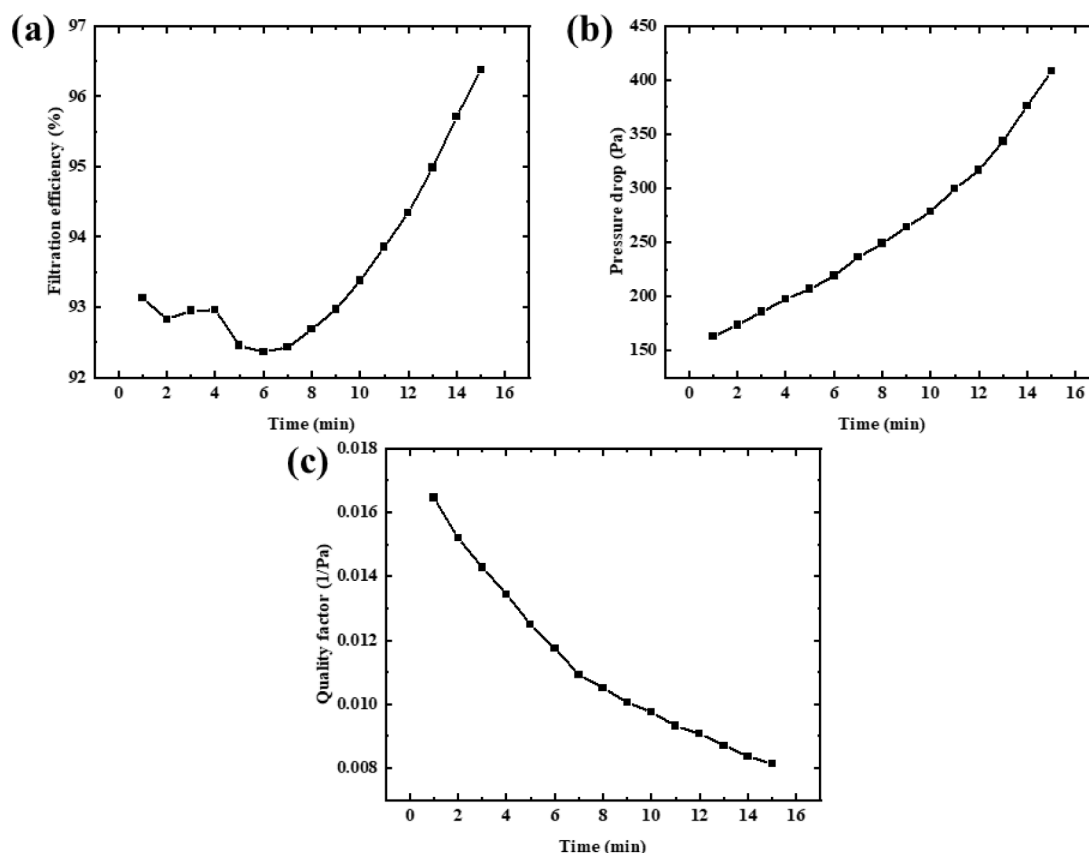


Fig. A2. Durability test of Model II (flow rate = 30 L min<sup>-1</sup>).

for aerosols carrying the COVID-19 virus was conducted. This affects the further design of the mask. Based on this existing problem, both experiment and numerical simulation were comparatively conducted to reveal how three-layer surgical masks prevent SARS-CoV-2 transmission. Here, a SEM technique was conducted to obtain the microstructure and distribution of spun-bond polypropylene nonwoven fabrics layers and melt-blown nonwoven polypropylene fabric layer of a commercial surgical mask currently in widespread use; on this basis, 3D computational models were built for performing CFD calculation. The numerical simulation was verified by comparing the experimental results in the present study and other researchers' theoretical works.

In the inner and outer layers of surgical mask, the fiber diameter of spun-bond polypropylene nonwoven fabric is measured to be approximately 20  $\mu\text{m}$ ; whereas in the middle layer, the fiber diameter of melt-blown nonwoven polypropylene fabric is statistically 3.06  $\mu\text{m}$ . The solid volume fraction of spun-bond polypropylene nonwoven fabric and melt-blown nonwoven polypropylene fabric are 11.23% and 41.53%, respectively. The measurement shows middle layer contributes more than 90% of the respiratory resistance, but it plays a major role in particle filtration, the highest filtration contribution rate can reach 95%. It was found for particles > 1.0  $\mu\text{m}$  in diameter, an increase in particle size leads to increase in filtration efficiency; whereas for particles < 0.3  $\mu\text{m}$  in diameter, filtration efficiency decreased as the particle size increased. In the size regime less than 0.3  $\mu\text{m}$ , the three-layer surgical mask has extremely low filtration efficiency, with the maximum filtration efficiency being only 30%. It was also found the filtration efficiency for larger particles (> 1.0  $\mu\text{m}$  in diameter) increased considerably with an increase in particle density, whereas that for smaller particles (< 1.0  $\mu\text{m}$  in diameter) did not demonstrate any such relationship. The numerical simulation shows three-layer surgical mask achieves the lowest filtration efficiency (~15%) for particles with diameters of approximately 0.3  $\mu\text{m}$ , which is consistent with other researchers' findings.

#### CRediT authorship contribution statement

**Z. Han:** Conceptualization, Methodology, Software, Writing – original draft, Writing – review & editing. **L. Wang:** Investigation, Resources, Methodology, Software. **Y. Liu:** Investigation, Resources. **T.L. Chan:** Formal analysis, Visualization. **Z. Shi:** Investigation, Resources. **M. Yu:** Investigation, Resources, Funding acquisition, Project administration, Methodology, Writing - review & editing.

#### Declaration of Competing Interest

The authors declare that they have no known competing financial interests or personal relationships that could have appeared to influence the work reported in this paper.

#### Data availability

No data was used for the research described in the article.

#### Acknowledgements

The authors thank the Natural Science Foundation of China of Zhejiang Province (LZ22A020004) for their support.

#### Appendix A

Each layer of fiber medium in Model II is divided at equal intervals, and the pressure drop of fiber medium at equal intervals is measured. As shown in Appendix Fig. A1, the pressure drop of each layer of fiber medium presents a linear distribution.

In order to test the durability of surgical masks, a clean surgical mask was placed on the filtration efficiency test bench (Fig. 6a) and subjected

to airflow loading of different duration. The test results are shown in Appendix Fig. A2. It can be seen that with the increase of time, the filtration efficiency and pressure drop of fiber filter material increases significantly, and the quality factor decreases gradually. This is because more aerosols are attached to the surface of the fiber, blocking part of the pores of the fiber medium, causing a large pressure difference and reducing the quality factor of the fiber medium. Therefore, we recommend that surgical masks be disposable.

## References

- [1] S.E. Eikenberry, M. Mancuso, E. Iboi, T. Phan, K. Eikenberry, Y. Kuang, E. Kostelich, A.B. Gumel, To mask or not to mask: Modeling the potential for face mask use by the general public to curtail the COVID-19 pandemic, *Infect. Dis. Model.* 5 (2020) 293–308, <https://doi.org/10.1016/j.idm.2020.04.001>.
- [2] S. Tang, Y. Mao, R.M. Jones, Q. Tan, J.S. Ji, N.A. Li, J. Shen, Y. Lv, L. Pan, P. Ding, X. Wang, Y. Wang, C.R. MacIntyre, X. Shi, Aerosol transmission of SARS-CoV-2? Evidence, prevention and control, *Environ. Int.* 144 (2020) 106039.
- [3] K.O. Dowd, K.M. Nair, P. Forouzandeh, S. Mathew, J. Grant, R. Moran, J. Bartlett, J. Bird, S.C. Pillai, Face Masks and Respirators in the Fight Against the COVID-19 Pandemic: A Review of Current Materials, *Adv. Future Perspect.* 2 (2020).
- [4] Americans Are Now Learning What People in East Asia Already Knew About Masks - The New York Times, (n.d.). <https://www.nytimes.com/2022/01/15/world/c-hina-masks-usa.html> (accessed July 27, 2022).
- [5] Masks Save Lives: Duke Study Confirms Which Ones Work Best | Hartford HealthCare | CT, (n.d.). <https://hartfordhealthcare.org/about-us/news-press/news-detail?articleid=27691&publicid=395> (accessed July 27, 2022).
- [6] Who, Infection prevention and control in the context of coronavirus disease (COVID-19): A living guideline, *World Heal. Organ.* (2022) 1–74.
- [7] W. Du, F. Iacoviello, T. Fernandez, R. Loureiro, D.J.L. Brett, P.R. Shearing, Microstructure analysis and image-based modelling of face masks for COVID-19 virus protection, *Commun. Mater.* 2 (2021), <https://doi.org/10.1038/s43246-021-00160-z>.
- [8] W.C. Su, J. Lee, J. Xi, K. Zhang, Investigation of Mask Efficiency for Loose-fitting Masks against Ultrafine Particles and Effect on Airway Deposition Efficiency, *Aerosol. Air QCL. Res.* 22 (2022) 1–14, <https://doi.org/10.4209/AAQR.210228>.
- [9] J. Zhang, H. Wang, C. Chen, A.n. Gui, X. Zhang, Y. Wang, Y.i. Xiong, W. Zeng, Analysis of microstructure and protective performance of melt-blown materials for medical protective masks, *J. Phys. Conf. Ser.* 2194 (1) (2022) 012010.
- [10] Y. Sheng, M. Wang, L. Zhang, Q. Ren, Analysis of filtration process of 3-D mesh spacer filter by using CFD-DEM simulation, *Powder Technol.* 396 (2022) 785–793, <https://doi.org/10.1016/j.powtec.2021.11.034>.
- [11] C. Tsutsumi-Arai, Y. Iwamiya, R. Hoshino, C. Terada-Ito, S. Sejima, K. Akutsu-Suyama, M. Shibayama, Z. Hiroi, R. Tokuyama-Toda, R. Iwamiya, K. Ijichi, T. Chiba, K. Satomura, Surface Functionalization of Non-Woven Fabrics Using a Novel Silica-Resin Coating Technology: Antiviral Treatment of Non-Woven Fabric Filters in Surgical Masks, *Int. J. Environ. Res. Public Health.* 19 (2022) 1–10, <https://doi.org/10.3390/ijerph19063639>.
- [12] A. Tcharkhtchi, N. Abbasnezhad, M. Zarbini Seydani, N. Zirak, S. Farzaneh, M. Shirinbayan, An overview of filtration efficiency through the masks: Mechanisms of the aerosols penetration, *Bioact. Mater.* 6 (2021) 106–122, <https://doi.org/10.1016/j.bioactmat.2020.08.002>.
- [13] E.K. Buami, C. Kumah, D. Vigbedor, R.M. Tsotorvor, R. Pan, Comparative Study of Polypropylene Non-Woven Surgical Mask and Locally Manufactured Woven and Knitted Fabrics Facial Masks, *J. Text. Sci. Technol.* 07 (2021) 131–141, <https://doi.org/10.4236/jtst.2021.73011>.
- [14] J. Pan, C. Harb, W. Leng, L.C. Marr, Inward and outward effectiveness of cloth masks, a surgical mask, and a face shield, *Aerosol. Sci. Technol.* 55 (2021) 718–733, <https://doi.org/10.1080/02786826.2021.1890687>.
- [15] N. El-Atab, N. Qaiser, H. Badghaish, S.F. Shaikh, M.M. Hussain, Flexible Nanoporous Template for the Design and Development of Reusable Anti-COVID-19 Hydrophobic Face Masks, *ACS Nano* 14 (6) (2020) 7659–7665.
- [16] Z. Sun, J. Wen, X. Luo, W. Du, Z. Liang, K. Fu, An improved CFD model of gas flow and particle interception in a fiber material, *Chin. J. Chem. Eng.* 25 (2017) 264–273, <https://doi.org/10.1016/j.cjche.2016.08.026>.
- [17] A. Karadimos, R. Ocone, The effect of the flow field recalculation on fibrous filter loading: A numerical simulation, *Powder Technol.* 137 (2003) 109–119, [https://doi.org/10.1016/S0032-5910\(03\)00132-3](https://doi.org/10.1016/S0032-5910(03)00132-3).
- [18] T. Müller, J. Meyer, G. Kasper, Low Reynolds number drag and particle collision efficiency of a cylindrical fiber within a parallel array, *J. Aerosol. Sci.* 77 (2014) 50–66, <https://doi.org/10.1016/j.jaerosci.2014.07.007>.
- [19] C. Kanaoka, H. Emi, T. Myojo, Simulation of the growing process of a particle dendrite and evaluation of a single fiber collection efficiency with dust load, *J. Aerosol. Sci.* 11 (4) (1980) 377–389.
- [20] O. Filippova, D. Hänel, Lattice-Boltzmann simulation of gas-particle flow in filters, *Comput. Fluids.* 26 (1997) 697–712, [https://doi.org/10.1016/S0045-7930\(97\)00009-1](https://doi.org/10.1016/S0045-7930(97)00009-1).
- [21] S.A. Hosseini, H. Vahedi Tafreshi, Modeling particle-loaded single fiber efficiency and fiber drag using ANSYS-Fluent CFD code, *Comput. Fluids.* 66 (2012) 157–166, <https://doi.org/10.1016/j.compfluid.2012.06.017>.
- [22] L. Zhang, JiaWei Zhou, B.o. Zhang, W. Gong, Semi-analytical and computational investigation of different fibrous structures affecting the performance of fibrous media, *Sci. Prog.* 103 (1) (2020), <https://doi.org/10.1177/0036850419874231>.
- [23] B. Cao, S. Wang, W. Dong, J. Zhu, F. Qian, J. Lu, Y. Han, Investigation of the filtration performance for fibrous media: Coupling of a semi-analytical model with CFD on Voronoi-based microstructure, *Sep. Purif. Technol.* 251 (2020) 117364, <https://doi.org/10.1016/j.seppur.2020.117364>.
- [24] B. Maze, H. Vahedi Tafreshi, Q. Wang, B. Pourdeyhi, A simulation of unsteady-state filtration via nanofiber media at reduced operating pressures, *J. Aerosol. Sci.* 38 (2007) 550–571, <https://doi.org/10.1016/j.jaerosci.2007.03.008>.
- [25] J. Roegiers, S. Denys, Development of a novel type activated carbon fiber filter for indoor air purification, *Chem. Eng. J.* 417 (2021) 128109, <https://doi.org/10.1016/j.cej.2020.128109>.
- [26] C. Yue, Q. Zhang, Z. Zhai, Numerical simulation of the filtration process in fibrous filters using CFD-DEM method, *J. Aerosol. Sci.* 101 (2016) 174–187, <https://doi.org/10.1016/j.jaerosci.2016.08.004>.
- [27] A.M. Saleh, S.A. Hosseini, H. Vahedi Tafreshi, B. Pourdeyhi, 3-D microscale simulation of dust-loading in thin flat-sheet filters: A comparison with 1-D macroscale simulations, *Chem. Eng. Sci.* 99 (2013) 284–291, <https://doi.org/10.1016/j.ces.2013.06.007>.
- [28] P.C. Gervais, D. Bémer, S. Bourrous, L. Ricciardi, Airflow and particle transport simulations for predicting permeability and aerosol filtration efficiency in fibrous media, *Chem. Eng. Sci.* 165 (2017) 154–164, <https://doi.org/10.1016/j.ces.2017.03.002>.
- [29] Q. Wang, B. Maze, H.V. Tafreshi, B. Pourdeyhi, A case study of simulating submicron aerosol filtration via lightweight spun-bonded filter media, *Chem. Eng. Sci.* 61 (2006) 4871–4883, <https://doi.org/10.1016/j.ces.2006.03.039>.
- [30] T.M. Bucher, H.V. Tafreshi, G.C. Tepper, Modeling performance of thin fibrous coatings with orthogonally layered nanofibers for improved aerosol filtration, *Powder Technol.* 249 (2013) 43–53, <https://doi.org/10.1016/j.powtec.2013.07.023>.
- [31] Y. Lin, R. Bahreini, S. Zimmerman, E.A. Fofie, A. Asa-Awuku, K. Park, S.B. Lee, G. N. Bae, H.S. Jung, Investigation of ambient aerosol effective density with and without using a catalytic stripper, *Atmos. Environ.* 187 (2018) 84–92, <https://doi.org/10.1016/j.atmosenv.2018.05.063>.
- [32] J. Rissler, E.Z. Nordin, A.C. Eriksson, P.T. Nilsson, M. Frosch, M.K. Sporre, A. Wierzbicka, B. Svenningsson, J. Löndahl, M.E. Messing, S. Sjogren, J. G. Hemmingsen, S. Loft, J.H. Pagels, E. Swietlicki, Effective density and mixing state of aerosol particles in a near-traffic urban environment, *Environ. Sci. Technol.* 48 (2014) 6300–6308, <https://doi.org/10.1021/es5000353>.
- [33] Z. Yin, X. Ye, S. Jiang, Y. Tao, Y. Shi, X. Yang, J. Chen, Size-resolved effective density of urban aerosols in Shanghai, *Atmos. Environ.* 100 (2015) 133–140, <https://doi.org/10.1016/j.atmosenv.2014.10.055>.
- [34] S. Adanur, A. Jayswal, Filtration mechanisms and manufacturing methods of face masks: An overview, *J. Ind. Text.* 51 (3 suppl) (2022), 3683 S–3717S.
- [35] S. Subramaniam, Lagrangian-Eulerian methods for multiphase flows, *Prog. Energy Combust. Sci.* 39 (2013) 215–245, <https://doi.org/10.1016/j.pecs.2012.10.003>.
- [36] F. Qian, N. Huang, X. Zhu, J. Lu, Numerical study of the gas-solid flow characteristic of fibrous media based on SEM using CFD-DEM, *Powder Technol.* 249 (2013) 63–70, <https://doi.org/10.1016/j.powtec.2013.07.030>.
- [37] S.H. Woo, S.C. Lee, S.J. Yook, Statistical Lagrangian particle tracking approach to investigate the effect of thermophoresis on particle deposition onto a face-up flat surface in a parallel airflow, *J. Aerosol. Sci.* 44 (2012) 1–10, <https://doi.org/10.1016/j.jaerosci.2011.10.003>.
- [38] Y. Huang, X. Zhao, Y. Pan, Slip-shear and inertial migration of finite-size spheres in plane Poiseuille flow, *Comput. Mater. Sci.* 176 (2020) 109542, <https://doi.org/10.1016/j.commatsci.2020.109542>.
- [39] S.A. Morsi, A.J. Alexander, An investigation of particle trajectories in two-phase flow systems, *J. Fluid Mech.* 55 (1972) 193–208, <https://doi.org/10.1017/S0022112072001806>.
- [40] X. Liu, X. Ding, C. Chen, R. An, W. Guo, W. Zhang, H. Nan, Y. Wang, Investigating the filtration behavior of metal fiber felt using CFD-DEM simulation, *Eng. Appl. Comput. Fluid Mech.* 13 (2019) 426–437, <https://doi.org/10.1080/19942060.2019.1608306>.
- [41] J. Roegiers, S. Denys, CFD-modelling of activated carbon fibers for indoor air purification, *Chem. Eng. J.* 365 (2020) 80–87, <https://doi.org/10.1016/j.cej.2019.02.007>.
- [42] X. Tian, Q. Ou, J. Liu, Y. Liang, D.Y.H. Pui, Influence of pre-stage filter selection and face velocity on the loading characteristics of a two-stage filtration system, *Sep. Purif. Technol.* 224 (2019) 227–236.
- [43] R. Tao, M. Yang, S. Li, Effect of adhesion on clogging of microparticles in fiber filtration by DEM-CFD simulation, *Powder Technol.* 360 (2020) 289–300, <https://doi.org/10.1016/j.powtec.2019.09.083>.
- [44] J. Happel, Viscous flow relative to arrays of cylinders, *AIChE J.* 5 (1959) 174–177, <https://doi.org/10.1002/aic.690050211>.
- [45] S. Kuwabara, The forces experienced by randomly distributed parallel circular cylinders, *J. Phys. Soc. Japan.* 14 (1959) 527–532.
- [46] C.N. Davies, Air Filtration, 1973.
- [47] N. Rao, M. Faghri, Computer modeling of aerosol filtration by fibrous filters, *Aerosol. Sci. Technol.* 8 (1988) 133–156, <https://doi.org/10.1080/02786828808959178>.
- [48] M.A. Hassan, B.Y. Yeom, A. Wilkie, B. Pourdeyhi, S.A. Khan, Fabrication of nanofiber meltblown membranes and their filtration properties, *J. Memb. Sci.* 427 (2013) 336–344, <https://doi.org/10.1016/j.memsci.2012.09.050>.
- [49] A. Podgórski, A. Balazy, L. Gradoń, Application of nanofibers to improve the filtration efficiency of the most penetrating aerosol particles in fibrous filters, *Chem. Eng. Sci.* 61 (2006) 6804–6815, <https://doi.org/10.1016/j.ces.2006.07.022>.

- [50] X. Zhang, J. Liu, H. Zhang, J. Hou, Y. Wang, C. Deng, C. Huang, X. Jin, Multi-layered, corona charged melt blown nonwovens as high performance pm0.3 air filters, *Polymers (Basel)* 13 (2021) 1–14, <https://doi.org/10.3390/polym13040485>.
- [51] R.S. Barhate, S. Ramakrishna, Nanofibrous filtering media: Filtration problems and solutions from tiny materials, *J. Memb. Sci.* 296 (2007) 1–8, <https://doi.org/10.1016/j.memsci.2007.03.038>.
- [52] R. Thakur, D. Das, A. Das, Electret air filters, *Sep. Purif. Rev.* 42 (2013) 87–129, <https://doi.org/10.1080/15422119.2012.681094>.
- [53] A. Karakoç, A. Miettinen, E. Sözümert, L. Evans, H. Yigitler, B. Bostanci, E. Taciroğlu, R. Jäntti, Microstructural evaluation and recommendations for face masks in community use to reduce the transmission of respiratory infectious diseases, *Comput. Methods Programs Biomed.* 226 (2022) 107154.
- [54] J.-S. Benas, C.-Y. Huang, Z.-L. Yan, F.-C. Liang, P.-Y. Li, C.-H. Lee, Y.-Y. Yu, C.-W. Chen, C.-C. Kuo, Nanofiber-Based Odor-Free Medical Mask Fabrication Using Polyvinyl Butyral and Eucalyptus Anti Odor Agent, *Polymers (Basel)* 14 (2022) 4447.
- [55] B. Cao, F. Qian, M. Ye, Y. Guo, S. Wang, J. Lu, Y. Han, Pressure drop model for fibrous media in depth filtration: Coupling simulation of microstructure and CFD porous media during dust loading, *Build. Environ.* 202 (2021) 108015, <https://doi.org/10.1016/j.buildenv.2021.108015>.
- [56] M. Tang, J. Hu, Y. Liang, D.Y.H. Pui, Pressure drop, penetration and quality factor of filter paper containing nanofibers, *Text. Res. J.* 87 (2017) 498–508, <https://doi.org/10.1177/0040517516631318>.
- [57] N. Galka, A. Saxena, High efficiency air filtration: The growing impact of membranes, *Filtr. Sep.* 46 (2009) 22–25, [https://doi.org/10.1016/S0015-1882\(09\)70157-0](https://doi.org/10.1016/S0015-1882(09)70157-0).
- [58] S.-B. Kwon, J. Park, J. Jang, Y. Cho, D.-S. Park, C. Kim, G.-N. Bae, A.m. Jang, Study on the initial velocity distribution of exhaled air from coughing and speaking, *Chemosphere* 87 (11) (2012) 1260–1264.
- [59] C.-J. Cho, Y.-S. Chang, Y.-Z. Lin, D.-H. Jiang, W.-H. Chen, W.-Y. Lin, C.-W. Chen, S.-P. Rwei, C.-C. Kuo, Green electrospun nanofiber membranes filter prepared from novel biomass thermoplastic copolyester: Morphologies and filtration properties, *J. Taiwan Inst. Chem. Eng.* 106 (2020) 206–214.